cm CHEMISTRY OF MATERIALS

Article

pubs.acs.org/cm

High-Figure-of-Merit Thermoelectric La-Doped A-Site-Deficient $SrTiO_3$ Ceramics

Zhilun Lu, Huairuo Zhang, Wen Lei, Derek C. Sinclair, and Ian M. Reaney*

Department of Materials Science & Engineering, University of Sheffield, Sheffield S1 3JD, United Kingdom

ABSTRACT: The structure and thermoelectric (TE) properties of La-doped, A-site-deficient $SrTiO_3$ ($Sr_{1-3x/2}La_xTiO_3$) ceramics sintered in air and N_2/5% H_2 have been investigated. Air-sintered ceramics with $0.10 \leq x < 0.30$ appear cubic by X-ray diffraction (XRD) but exhibit superstructure consistent with a tetragonal cell ($a^0a^0c^-$), according to electron diffraction (ED) studies. $0.30 \leq x < 0.50$ have additional short-range A-site vacancy (V_A) ordering, and $x \geq 0.50$ are orthorhombic with an $a^-a^-c^+$ tilt system and long-range V_A ordering. $0.10 \leq x \leq 0.50$ reduced in N_2/5% H_2 are oxygen-deficient and appear cubic in XRD patterns but exhibit superstructure compliant with an $a^0a^0c^-$ tilt system by ED. For $x = 0.50$, additional short-range V_A order is observed, and $x > 0.50$ are orthorhombic with an $a^-a^-c^+$ tilt system and long-range V_A ordering. $x = 0.15$ sintered in N_2/5% H_2 shows the largest dimensionless TE figure-of-merit $ZT = 0.41$ at 973 K reported for n-type $SrTiO_3$-based ceramics, suggesting that the accommodation of La through formation of (V_{Sr}) coupled with reduction in N_2/5% H_2 represents a new protocol for the development of oxide-based thermoelectrics.

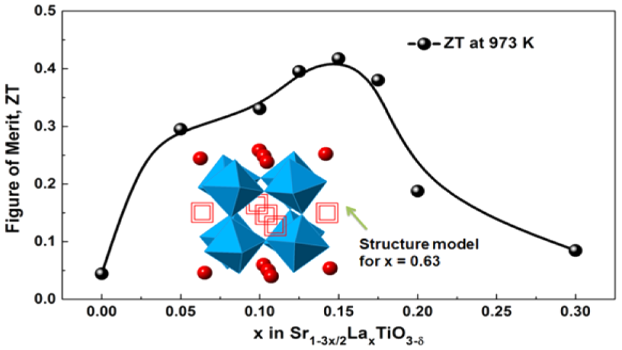

1. INTRODUCTION

Thermoelectric generators (TEGs) can convert heat into electricity directly and vice versa and have emerged as a promising new technology for energy harvesting and refrigeration. Most state-of-the-art thermoelectrics with high figure-of-merit ($ZT = S^2\sigma/\kappa$, where S is the Seebeck coefficient, σ is electrical conductivity, and κ is thermal conductivity) values are composed of toxic, naturally rare, and heavy metal elements.[1] As a result, further work is required to develop new, low-cost, stable materials based on oxides. Excellent properties have already been reported for layered cobaltite-based thermoelectrics such as Na_xCoO_2 ($ZT \sim 1$), which exhibit p-type conductivity.[2] To date, n-type oxides with equivalent ZT values have yet to be discovered.[3] $SrTiO_3$-based systems have attracted considerable attention due to their high thermoelectric properties by so-called donor-doping with higher valence ions on the A- or B-site,[4−6] especially lanthanum-doped $SrTiO_3$ (LST).[4,5] Table 1 summarizes the reported properties for several doped $SrTiO_3$ thermoelectric materials.

Reports for LST are inconsistent and contradictory with respect to the doping mechanisms, solid solution limits, and crystal symmetry, due, in part, to the sensitivity of LST samples to processing variables such as temperature, P_{O_2}, and time. To date, the weight of scientific evidence suggests that the extra positive charge from substitution of Sr^{2+} by La^{3+} is compensated by electrons offered by the creation of an equal number of Ti^{3+} from Ti^{4+} with a formula of $Sr_{1-x}{}^{2+}La_x{}^{3+}Ti_{1-x}{}^{4+}Ti_x{}^{3+}O_3$ under highly reducing conditions.[19−21] $Sr_{1-x}La_xTiO_3$ has, therefore, been widely studied as a promising candidate for thermoelectric applications.[22]

Table 1. Thermoelectric Properties of Doped $SrTiO_3$

composition	processing conditions	ZT
$Sr_{0.90}Dy_{0.10}TiO_3$[7]	Ar flow, 1873 K, 4 h	0.22, 573 K
$SrTi_{0.80}Nb_{0.20}O_3$ epitaxial film[8]	pulsed laser deposition, 973 K, on (100)-oriented $LaAlO_3$ single-crystalline substrates	0.37, 1000 K
$SrTi_{0.90}Ta_{0.10}O_3$[9]	dynamic vacuum, 1773 K, 16 h	0.17, 752 K
$Sr_{0.92}La_{0.08}TiO_3$[10]	spark plasma sintering, 1573 K, 5 min, 34 MPa in vacuum	0.37, 1045 K
$Sr_{0.90}Nd_{0.10}TiO_3$[11]	Ar/5% H_2, 1733 K, 4 h	0.28, 873 K
$Sr_{0.92}La_{0.08}TiO_3$[12]	spark plasma sintering, 1573 K, 30 min, 34 MPa in vacuum	0.22, 800 K
$Sr_{0.88}La_{0.12}TiO_3$[13]	Ar/5% H_2, 1273 K, 6 h, then Ar, 1673 K, 4 h	0.28, 773 K
$SrTi_{0.85}Nb_{0.15}O_3$ with 3 wt % YSZ[14]	Ar flow, 1773 K, 3 h	0.21, 900 K
$Sr_{0.80}La_{0.08}Dy_{0.12}TiO_3$[15]	Ar/5% H_2, 1733 K, 4 h	0.36, 1076 K
$Sr_{0.80}La_{0.13}Ti_{0.95}Nb_{0.05}TiO_3$[16]	N_2/5% H_2, 1723 K, 10 h	~0.30, 1000 K
$Sr_{0.55}Pr_{0.30}TiO_3$[17]	N_2/10% H_2, 1773 K, 10 h	~0.30, 1173 K
$Sr_{0.97}Ti_{0.8}Nb_{0.17}W_{0.03}O_3$[18]	N_2/10% H_2, 1773 K, 10 h	0.28, 1270 K

In contrast, there is little evidence to suggest that ionic compensation for La occurs through the formation of V_{Ti}.

Received: November 30, 2015
Revised: January 6, 2016
Published: January 7, 2016

DOI: 10.1021/acs.chemmater.5b04616
Chem. Mater. 2016, 28, 925−935

Instead, investigators have primarily focused on compositions in which La is compensated through the formation of A-site vacancies, according to the general formula $Sr_{1-3x/2}La_xTiO_3$, for potential use as anodes in solid oxide fuel cells.[23,24]

Several structural characterization studies of the $SrTiO_3$–$La_{2/3}TiO_3$ system have already been carried out. Battle et al. reported A-site cation-vacancy ordering in $Sr_{1-3x/2}La_xTiO_3$ ($0.25 \leq x \leq 0.60$) sintered in air using HRTEM.[25] At room temperature, $0.00 \leq x \leq 0.40$ are cubic and then orthorhombic ($Pban$) for $x = 0.50$ and 0.60, with the symmetry being dominated by long-range A-site vacancy ordering. In 2004, Howard et al. additionally concluded the existence of a sequence of octahedral tilt transitions in this system with a cubic room-temperature structure for $x < 0.20$, tetragonal ($I4/mcm$) for $x = 0.50$ with short-range cation-vacancy occurring for $0.30 \leq x \leq 0.50$, and then orthorhombic ($Cmmm$) for $x = 0.55$ with long-range A-site vacancy ordering present for $x \geq 0.55$.[26] Further studies on $Sr_{1-3x/2}La_xTiO_3$ suggested glass-like thermal conductivity when Nb is additionally substituted on the B-site and a large increase in power factor reported for Pr- and Nb-doped $SrTiO_3$ by Bos et al. and Kovalevsky et al., respectively.[16,17] In previous work, we have highlighted the importance of A-site vacancies in the oxygen-loss mechanism in $Sr_{1-3x/2}La_xTiO_3$,[27] according to eq 1, with A-site deficiency reported to improve the electrical conductivity in $Sr_{1-3x/2}La_xTiO_3$ as compared to that in $Sr_{1-x}La_xTiO_3$ for an equivalent P_{O_2} and temperature.[28,29]

$$O_O^x \rightarrow V_O^{\bullet\bullet} + 2e' + \frac{1}{2}O_2(g) \qquad (1)$$

Related studies on other materials such as ZnO have reported the influence of the preparation atmosphere on thermoelectric properties, which suggests that the formation of oxygen vacancies is conducive to the improvement of their n-type thermoelectric properties.[30,31]

There is, however, still no definitive report on the influence of cation/vacancy ordering, oxygen loss, and octahedral tilting on the thermoelectric properties of $Sr_{1-3x/2}La_xTiO_3$ oxides. Here, we compare the crystal structure of $Sr_{1-3x/2}La_xTiO_3$ ceramics sintered in air and N_2/5% H_2, with the intention of optimizing their thermoelectric properties at intermediate temperatures (673–973 K).

2. EXPERIMENTAL SECTION

A solid-state reaction method was used to prepare $Sr_{1-3x/2}La_xTiO_3$ ceramics from $SrCO_3$ (99.90%, Sigma-Aldrich), La_2O_3 (99.99%, Sigma-Aldrich), and TiO_2 (99.90%, Sigma-Aldrich). Stoichiometric amounts of dry raw powders were weighed and mixed using an attrition mill for 60 min with yttria-stabilized zirconia (YSZ) media in isopropanol. The mixed powders were calcined at 1373 K for 3 h in an alumina crucible after being dried at ∼80 °C and sieved. Pellets and bar samples were prepared using an uniaxial press with calcined powders, followed by cold isostatic pressing at 200 MPa and finally sintering in air at a cooling rate of 5 °C/min or flowing N_2/5% H_2 gas at a cooling rate of 30 °C/min at 1773 K for 6 h.

A high-resolution STOE STADI-P diffractometer (STOE & Cie GmbH, Darmstadt, Germany) with a linear position sensitive detector (PSD) with Cu Kα ($\lambda = 1.5406$ Å) radiation was used for crushed samples. Ceramic microstructures were studied using an FEI Inspect F scanning electron microscope (SEM). Samples for transmission electron microscopy (TEM) were ground and polished using SiC paper and then ion thinned to perforation using a Fischione low-angle ion milling system (model 1010, E.A. Fischione Instruments, Inc., USA). A Philips EM 420 (120 keV) transmission electron microscope was used to obtain electron diffraction (ED) patterns. A double-aberration-corrected microscope, JEM-Z3100F-R005 STEM/TEM, operated at 300 keV was employed to obtain high-angle annular dark field (HAADF) and annular bright field (ABF) images.

A PerkinElmer Pyris 1 TGA was used to measure the weight variation of ceramic samples as a function of temperature in air with a 5 °C/min heating rate up to 1000 °C and a 5 °C/min cooling rate to room temperature.

S and σ were measured simultaneously on $\sim 20 \times 3 \times 3$ mm^3 bar samples in air from 473 to 973 K by a conventional steady-state method and a four-probe method, respectively. κ measurements were performed on an Anter FlashlineTM 3000 with a high-speed xenon discharge (HSXD) pulse source.

3. RESULTS

3.1. Phase Assemblage and Grain Structure.

$Sr_{1-3x/2}La_xTiO_3$ ceramics sintered in air exhibited only peaks associated with a perovskite phase for $x \leq 0.63$, above which intensities associated with a $La_2Ti_2O_7$ phase were observed (Figure 1a). Samples with $x \leq 0.40$ appeared cubic by XRD, but for $0.50 \leq x \leq 0.63$, splitting of the major perovskite peaks along with the appearance of superstructure reflections indicated an orthorhombic structure. Superlattice reflections relating to the orthorhombic structures are labeled O for the air-sintered samples. These peaks became sharper and more intense with increasing x. In contrast, samples sintered in N_2/5% H_2 exhibited only peaks associated with the perovskite phase for all compositions within the solid solution (Figure 1b). Although peak splitting was not observed for any composition, superstructure reflections are indicated for compositions with $x \geq 0.30$. Unit cell volume versus x of air- and N_2/5% H_2-sintered samples is plotted in Figure 1c. For air-sintered samples, the unit cell volume decreases with increasing x, consistent with the substitution of Sr (1.44 Å in CN12) with the smaller La ion (1.32 Å in CN12),[32] but it then drops precipitously at $x \sim 0.50$ and subsequently increases with a positive slope, concomitant with the onset of a transition to an orthorhombic structure. In contrast, the unit cell volume for samples sintered in N_2/5% H_2 increases from $x = 0.00$ to 0.20 but then decreases. The initial increase is attributed to oxygen loss from the lattice, eq 1, which results in partial reduction of Ti^{4+} (0.605 Å in CN6) to larger Ti^{3+} ions (0.67 Å in CN6). The change in slope of cell volume at $x \sim 0.20$ may relate to the onset of a structural transition, but the subtle interplay among the concentration of V_{Sr}, V_O, and Ti^{3+} as x increases and how this might affect unit cell volume cast doubt on such a simplistic interpretation; however, the change in slope is approximately coincident with the appearance of superstructure reflections in the room temperature XRD traces (Figure 1b).

As shown in Figure 2, all ceramics exhibited dense microstructures with few pores. Grain sizes typically vary from 1 to 10 μm. Although there are clear variations in grain size as a function of composition and processing conditions, the role of A-site and oxygen vacancies in grain growth is complex and beyond the scope of the current study.

3.2. Octahedral Tilting and A-Site Vacancy Ordering.

3.2.1. Air-Sintered Samples. ⟨100⟩, ⟨110⟩, ⟨111⟩ zone-axis electron diffraction patterns (ZADPs) from ceramics with x = 0.30, 0.50, and 0.63 sintered in air are shown in Figure 3. For x = 0.30, sharp discrete superstructure reflections of the type $^1/_2\{ooo\}$ are observed in ⟨110⟩ ZADPs (Figure 3), with no discrete sharp superstructure present in ⟨111⟩ or ⟨001⟩ ZADPs, which has also been observed for x = 0.10 (not shown). According to Woodward and Reaney,[33] the appearance of only $^1/_2\{ooo\}$ reflections indicates a perovskite crystal structure in

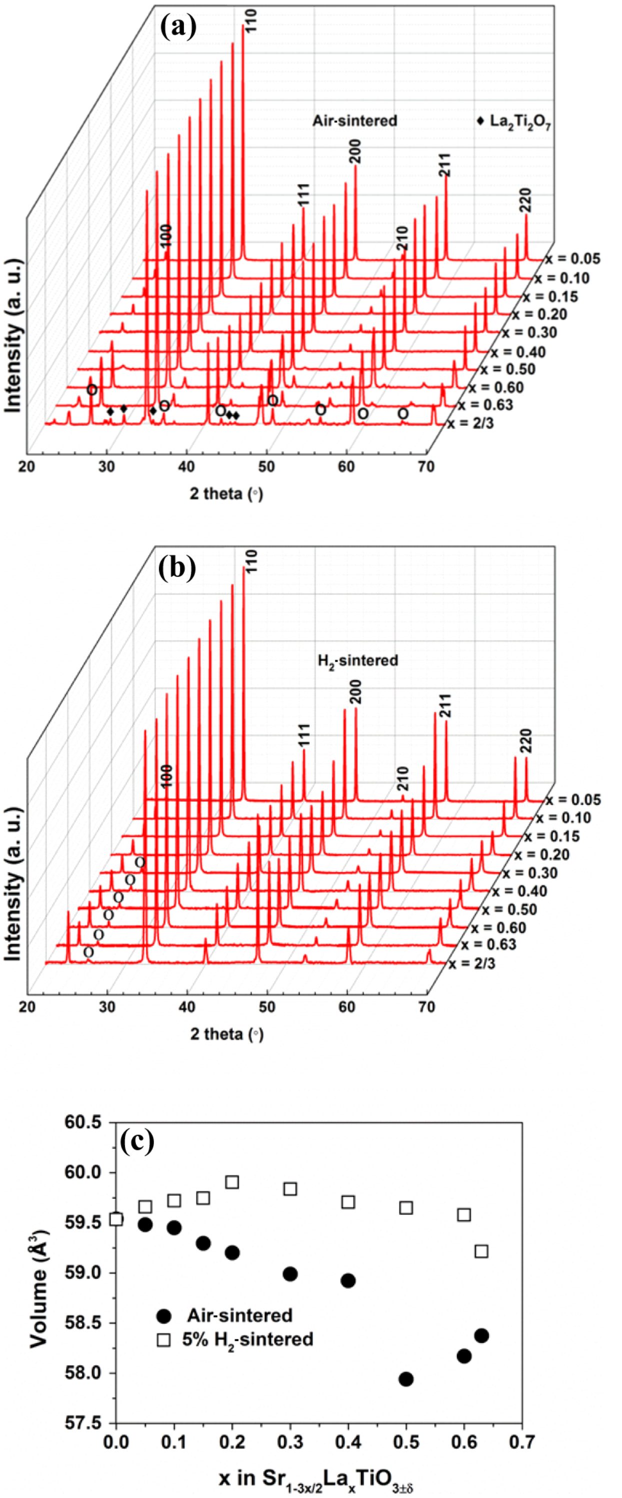

Figure 1. Room-temperature XRD patterns for $Sr_{1-3x/2}La_xTiO_3$ ceramics sintered at 1773 K for 6 h in (a) air or (b) N_2/5% H_2; (c) dependence of room-temperature cell volume with x.

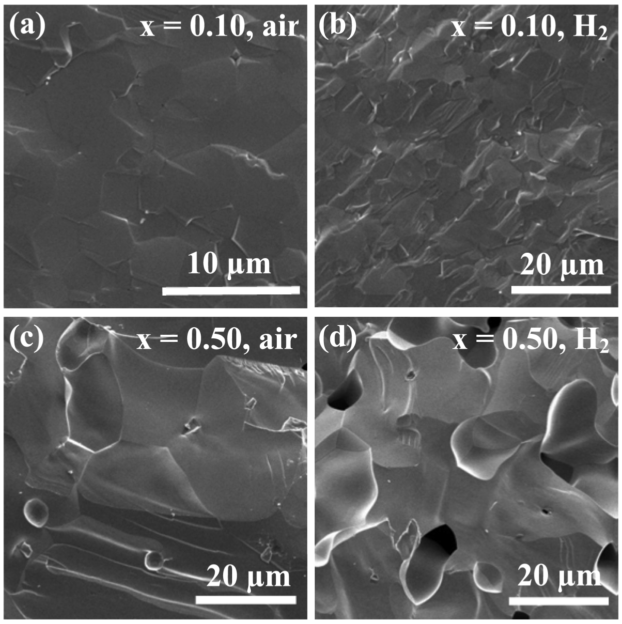

Figure 2. Secondary electron images of the fracture surfaces of $Sr_{1-3x/2}La_xTiO_3$ ceramics sintered at 1773 K for 6 h in air and N_2/5% H_2.

which the O octahedra are rotated in antiphase only, consistent with the tetragonal symmetry ($I4/mcm$) and $a^0a^0c^-$ Glazer tilt system reported for this composition by Howard et al.;[26,34] however, diffuse reflections are also observed for x = 0.30 at $^1/_2\{eeo\}$ positions. These reflections are unlikely to relate to octahedral tilting as $^1/_2\{eeo\}$ occur only when both in-phase and antiphase tilting are present.[33] It is more likely that the diffuse reflections relate to short-range order (SRO) of A-site vacancies on alternate (001) planes first proposed to exist in these compounds by Battle et al.[25]

For x = 0.50 and 0.63, superstructure reflections of the type $^1/_2\{ooe\}$ and $^1/_2\{eeo\}$ are observed in ⟨001⟩ and ⟨110⟩, and $^1/_2\{ooe\}$ is observed in ⟨111⟩ ZADPs (Figure 3). $^1/_2\{ooe\}$ and $^1/_2\{eeo\}$ reflections are conventionally associated with the presence of in-phase rotations of the O-octahedra and antiparallel cation displacements, respectively,[33] but this simplistic interpretation is complicated by the presence of long-range A-site vacancy order which, according to Battle et al., gives rise to primary superstructure reflections at $^1/_2\{eeo\}$.[25] Moreover, $^1/_2\{eeo\}$ superstructure reflections may undergo complex double diffraction routes to give rise to $^1/_2\{ooe\}$ if diffraction occurs from two domain variants of the vacancy-ordered structure. Care must be taken, therefore, in deconvoluting these two mechanisms for the generation of superstructure. From their intensity distributions and based on structural data presented by Battle et al. and Howard et al.,[25,26] it is reasonable to assume that there are contributions to the $^1/_2\{eeo\}$ reflections from both A-site vacancy ordering and antiparallel cation displacements for compositions with x = 0.50 and 0.63 (Figure 3).

To determine the primary origin of the $^1/_2\{ooe\}$ reflections, ⟨111⟩ zone axes (Figure 3) are particularly useful since these reflections cannot be generated by any known mechanism of double diffraction (NB $^1/_2\{eeo\}$ reflections are forbidden according to the Weiss zone law in ⟨111⟩ ZADPs).[33] It can therefore be concluded that the discrete sharp reflections in ⟨111⟩ ZADPs from x = 0.63 arise uniquely from in-phase rotations of the octahedra, consistent with the proposed tilt system ($a^-a^-c^+$) by Howard et al.[26] According to Glazer and Woodward and Reaney,[33,34] if one axis of the perovskite structure is tilted in-phase, e.g., $^1/_2(312)$ and $^1/_2(132)$ reflections (N.B. these reflections are the allowed reflections of the type $^1/_2\{ooe\}$ in ⟨111⟩ ZADPs) are observed in ⟨111⟩ zone axes, but $^1/_2(321)$, $^1/_2(123)$, $^1/_2(213)$, and $^1/_2(231)$

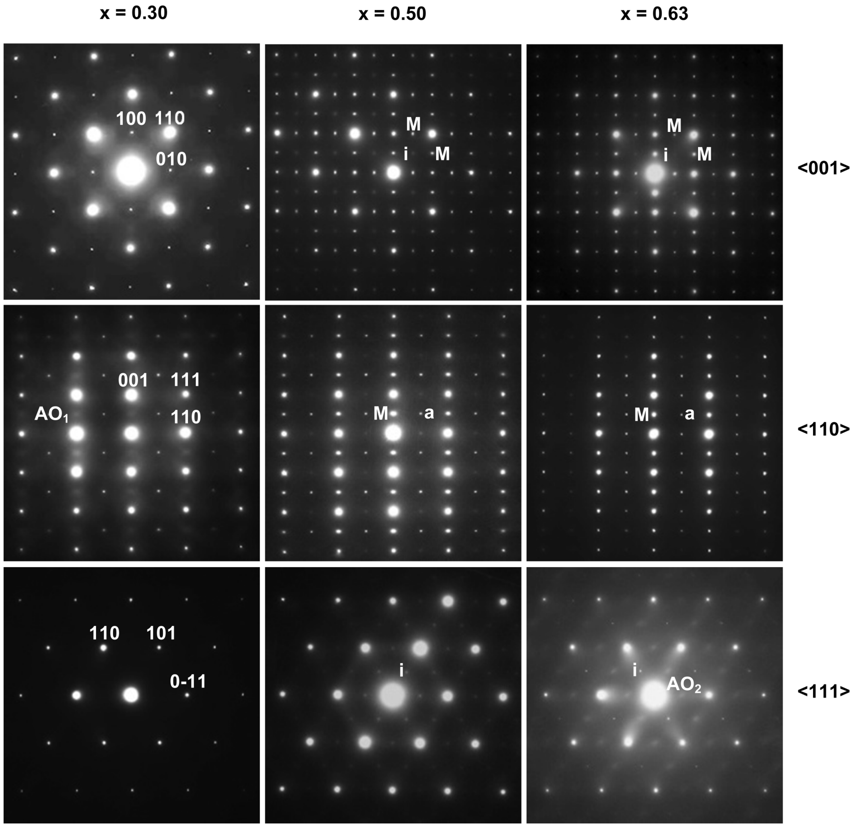

Figure 3. ⟨001⟩, ⟨110⟩, and ⟨111⟩ zone axis diffraction patterns from $Sr_{1-3x/2}La_xTiO_3$ ceramics sintered at 1773 K for 6 h in air. Superstructure reflections are indicated as follows: a = $^1/_2\{ooo\}$ antiphase tilt reflectionl i = $^1/_2\{eeo\}$ in-phase tilt reflection; AO_1 and AO_2 = $^1/_2\{eeo\}$ and $^1/_2\{ooe\}$ short-range vacancy ordering, respectively; and M = $^1/_2\{eeo\}$ with contributions from antiparallel cation displacements and long-range A-site vacancy order.

remain forbidden. All superstructure reflections of the type $^1/_2\{312\}$ are present in the ⟨111⟩ ZADP for $x = 0.50$ because diffraction has occurred equally from all potential domain variants of the $a^-a^-c^+$ tilt system.[33] The small ferroelastic twin domain width (20−50 nm) associated with $x = 0.50$ is shown in Figure 4. For $x = 0.63$, sharp, discrete reflections are observed only at $^1/_2(312)$, indicating diffraction from a single variant, the structure of which has one axis tilted in-phase, consistent with the tilt system ($a^-a^-c^+$) reported by Howard et al.[26] Single-domain diffraction patterns may be obtained from samples with $x = 0.63$ due to their larger domain width (0.5 μm) (Figure 4).

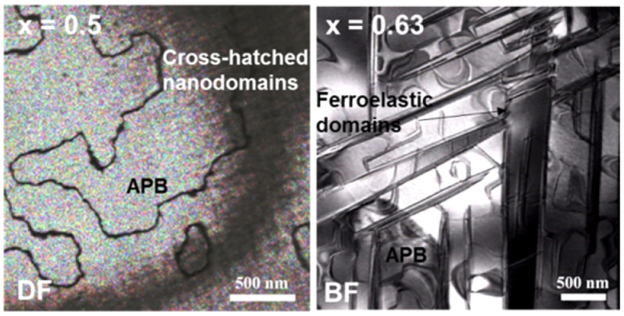

Figure 4. TEM images near ⟨110⟩ of $Sr_{1-3x/2}La_xTiO_3$ for ceramics with $x = 0.50$ and 0.63 sintered at 1773 K for 6 h in air. The dark field (DF) image reveals antiphase boundaries, APBs, associated with antiphase rotations of the O-octahedra. The bright field (BF) image shows ferroelastic domains due to the orthorhombic distortion and APBs relating to antiparallel cation displacements.

However, diffuse reflections of the type $^1/_2\{312\}$ are visible at all positions in ⟨111⟩ ZADPs from samples with $x = 0.63$, including diffuse halos around the sharp, discrete reflections at $^1/_2(312)$. The diffuse $^1/_2\{ooe\}$ reflections are most likely associated with A-site vacancy ordering, but $^1/_2\{312\}$ ($^1/_2\{ooe\}$) reflections are forbidden according to the structure model proposed by Battle et al.,[25] which generates superstructure reflections only of the type $^1/_2\{eeo\}$. The origin of these reflections, therefore, requires further explanation.

A calculation of the proportion of A-site vacancies with respect to the available A-sites with increasing x points to a simple scenario to explain the initial appearance of $^1/_2\{eeo\}$ followed by diffuse reflections at $^1/_2$\{ooe\}. As x increases ($x < 0.50$, < 25% A-site vacancies), A-site vacancies accrete randomly onto alternate (001) planes, resulting in the appearance of $^1/_2\{eeo\}$ superstructure reflections. The cell doubling mechanism is the scattering power difference between the alternate partially vacated and the essentially fully occupied (001) A-site planes. As x increases ($x \geq 0.50$, ≥ 25% A-site vacancies), the A-site vacancies not only order on alternate (001) planes but also begin to undergo short-range order, SRO, within the partially vacated planes that gives rise to weak diffuse intensities at $^1/_2\{ooe\}$ positions in ED patterns in addition to strong discrete reflections at $^1/_2\{eeo\}$.

Figure 4 reveals a dark field (DF) TEM image obtained near the ⟨110⟩ direction using $^1/_2\{ooo\}$ from antiphase rotations of the O-octahedra and a bright field (BF) TEM image near the ⟨110⟩ in which $^1/_2\{eeo\}$ reflections (A-site vacancies/antiparallel cation displacements) were preferentially excited. Figure 4

(DF) clearly illustrates the antiphase boundaries that form due to impingement of regions of antiphase tilt that have nucleated out of phase. Note also that there is a cross-hatched background contrast in Figure 4 (DF) that arises from ferroelastic twin domains. The twin domains are approximately 20−50 nm and give rise to the multidomain electron diffraction patterns discussed above in the context of the ⟨111⟩ zone axis in Figure 3. In contrast, the twin domains for $x = 0.63$ are much larger and permit single-domain diffraction data (Figure 4). Also visible in Figure 4 (BF) are antiphase boundaries that arise primarily from the impingement of regions of antiparallel cation displacements that have nucleated out of phase (a contribution to the image from regions of A-site vacancy order cannot be excluded since the $^1/_2\{eeo\}$ reflection that is dominant under the two-beam condition for the image contains intensities arising from both mechanisms for the generation of superstructure). Note that the antiphase domain width associated with antiparallel cation displacements (~500 nm) is typically less than that observed for antiphase domains that arise from antiphase tilting.

Due to the complexity of the inter-relation between A-site vacancy ordering and octahedral tilting, aberration-corrected scanning transmission electron microscopy (STEM) was performed on $Sr_{0.055}La_{0.63}TiO_3$ ceramics sintered in air. Aberration correction atomic resolution images obtained using a high-angle annular dark field (HAADF) detector are capable of imaging columns of atoms with a contrast that relates directly to the average mass of the nuclei. Hence, regions of antiparallel cation displacement and A-site vacancy order may be distinguished unambiguously since the latter will exhibit atomic columns in which the partially vacated {001} have lighter contrast than the fully occupied A-site planes.

Atomic resolution STEM images taken from two domains along pseudocubic ⟨110⟩ zone axes are shown in Figure 5. The A- and B-site cations can be readily identified in both HAADF and the corresponding annular bright field (ABF) images. Oxygen anions on each side of the B-site cations can also be identified in the ABF images. A-site vacancy ordering was not apparent in one of the two domains, presumably due to orientation of the ordered structure (Figure 5a,b), but in the other twin, {100} planes deficient in A-site cations can be readily identified. The alternate layers of greater and lesser occupancy of A-site cations on the {100} planes give rise to a doubling of the periodic spacing along the corresponding ⟨100⟩ direction (Figure 5c,d), which unambiguously illustrates the formation of long-range A-site vacancy order. To confirm this observation, A-site vacancy ordering was further studied along ⟨001⟩ zone axes.

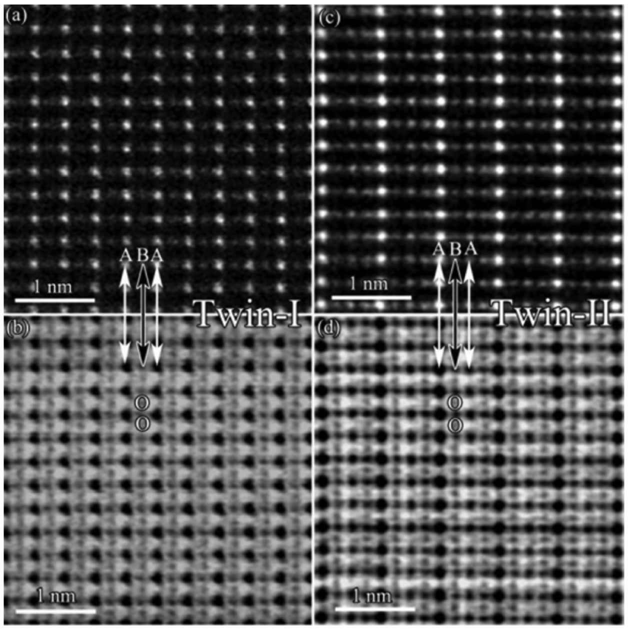

Figure 5. Pseudocubic ⟨110⟩ zone-axes atomic resolution HAADF-STEM images (a, c) and corresponding ABF-STEM images (b, d) taken from two domains of $Sr_{1-3x/2}La_xTiO_3$ ($x = 0.63$) ceramic sintered in air showing A-site vacancy ordering along the ⟨100⟩ direction. The white and black arrows illustrate A- and B-site crystallographic planes, respectively. Symbol O illustrates oxygen sites. Images are filtered to reduce the noise level.

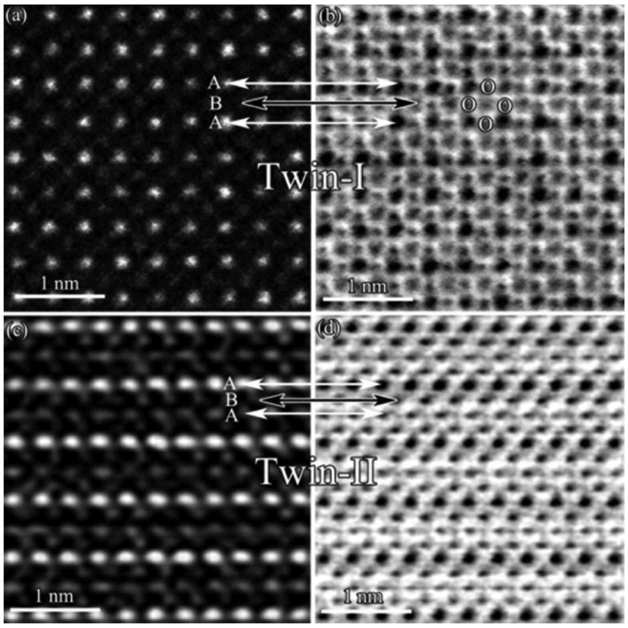

Figure 6. Pseudocubic ⟨001⟩ zone axes atomic resolution HAADF-STEM images (a, c) and corresponding ABF-STEM images (b, d) taken from two domains of $Sr_{1-3x/2}La_xTiO_3$ ($x = 0.63$) ceramic sintered in air showing A-site vacancy ordering in the ⟨100⟩ direction. The white and black arrows illustrate A- and B-site crystallographic planes, respectively. Symbol O illustrates oxygen sites. Images are filtered to reduce the noise level.

HAADF and ABF images of two domains taken along the ⟨001⟩ zone axes are shown in Figure 6. An atomic resolution HAADF image of one of the two domains is shown in Figure 6a, and a corresponding ABF image shown in Figure 6b. Besides the A/B sites, the oxygen site on the four sides of B-site cations can be readily identified in the ABF image, as shown by the O symbols in Figure 6b. There are some fluctuations in the intensity of the A-site columns, which may originate from the SRO that gives rise to diffuse $^1/_2\{ooe\}$ reflections in ⟨111⟩ zone axes, but no clear vacancy ordering that doubles {001} may be observed in this orientation of the lattice. In contrast, Figure 6c,d shows HAADF and ABF images of a second domain in which alternate A-site planes exhibit atomic columns of greater and lesser contrast, thereby indicating a doubling of periodic spacing along the corresponding ⟨100⟩ directions, which gives rise to $^1/_2\{eeo\}$ superstructure reflections in ED patterns. Once again, no evidence was observed to explain the weak, diffuse $^1/_2\{ooe\}$ reflections in ⟨111⟩ zone axes from samples with $x = 0.63$, but from their diffuse character and intensity, a clear contribution to an HAADF or ABF image is unlikely since nanometer scale SRO will average out through the thickness of the foil (5−10 nm).

Combining electron diffraction data with aberration-corrected images, a model of $Sr_{1-3x/2}La_xTiO_3$ (x = 0.63) can be constructed in which the tilt system is $a^-a^-c^+$ and in which alternate A-site planes contain a higher proportion of A-site vacancies (Figure 7).

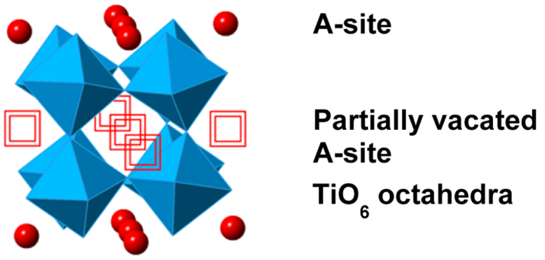

Figure 7. Structure model for $Sr_{1-3x/2}La_xTiO_3$ (x = 0.63) that combines an $a^-a^-c^+$ tilt system with alternate layer of A-site-deficient {001} planes. Within the {001} planes, A-site vacancies are randomly distributed; hence, a classic assignment of long-range symmetry is not attempted.

3.2.2. N_2/5% H_2-Sintered Samples. ⟨100⟩, ⟨110⟩, and ⟨111⟩ ZADPs obtained from x = 0.30, 0.50, and 0.63 sintered in N_2/5% H_2 are shown in Figure 8. For x = 0.30 and 0.50, the ⟨110⟩ ZADP exhibits strong, discrete $^1/_2\{ooo\}$ reflections with no other discrete superstructure reflections present in other major ZADPs. The tilt system is thus defined as being in antiphase only and is consistent with $I4/mcm$ symmetry ($a^0a^0c^-$) proposed by Howard et al. and also with the extra peak in XRD data at ~25.2° at $x \geq 0.30$.[26] Weak $^1/_2\{ooo\}$ reflections associated with antiphase tilting are also observed in ⟨110⟩ ZADPs of x = 0.10 and 0.15 (not shown here), indicating that the onset of octahedral tilting occurs at relatively low La concentrations. Diffuse intensities are also observed at $^1/_2\{eeo\}$ positions in ⟨001⟩ and ⟨110⟩ ZADPs (Figure 8). These reflections are associated with A-site vacancy ordering, but the onset of SRO occurs at x = 0.50 for N_2/5% H_2, in comparison with x = 0.30 for air-sintered samples.

For x = 0.63, superstructure reflections of the type $^1/_2\{ooe\}$ are observed in Figure 8, revealing the presence of in-phase rotations of O octahedra, consistent with an $a^-a^-c^+$ tilt system. The appearance of sharp, discrete $^1/_2\{ooe\}$ reflections and thus the onset of in-phase tilting occurs at lower values of x in air (x = 0.50) compared with that for N_2/5% H_2 (x = 0.63) sintered samples. The presence of SRO A-site vacancies for x = 0.50 (N_2/5% H_2) suggests that long-range order, LRO, should have developed for x = 0.63. However, the coincidence of reflections at $^1/_2(eeo)$ positions due to antiparallel cation displacements and A-site vacancy order prevents the presence of the latter from being unambiguously determined. Nonetheless, the weight of evidence suggests that A-site vacancy ordering occurs in N_2/5% H_2 but at higher values of x than in air-sintered samples.

The displacement of the onset of both in-phase tilting and A-site vacancy order to high values of x for N_2/5% H_2 compared with that of air-sintered samples is directly related to the

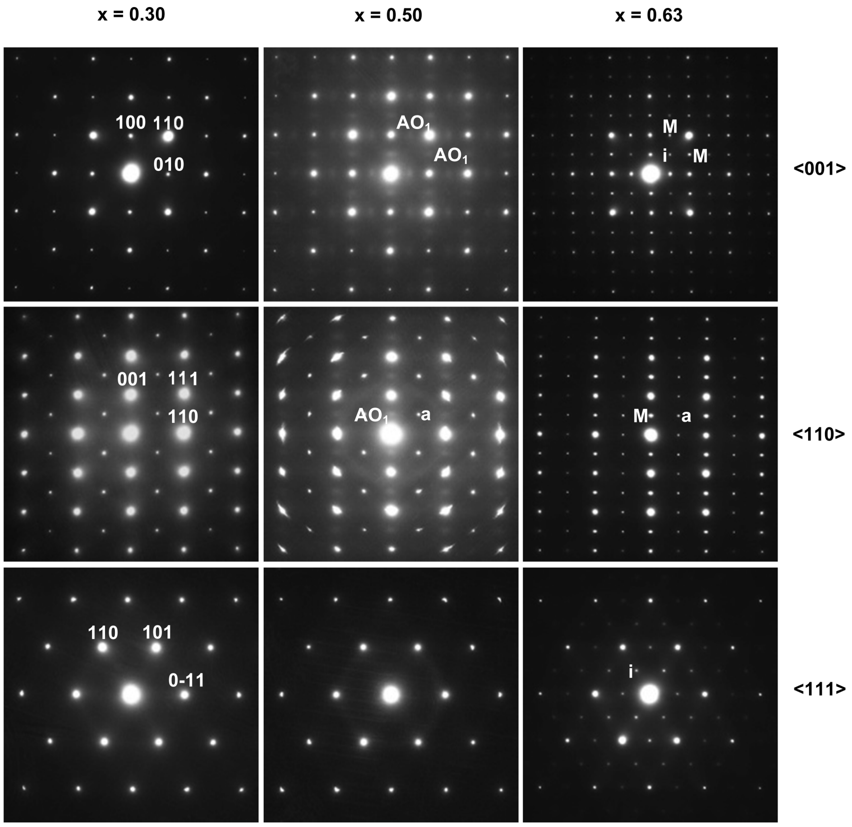

Figure 8. ⟨001⟩, ⟨110⟩, and ⟨111⟩ zone axis diffraction patterns from $Sr_{1-3x/2}La_xTiO_{3-\delta}$ ceramics sintered at 1773 K for 6 h in N_2/5% H_2. Superstructure reflections are indicated as follows: a = $^1/_2\{ooo\}$ antiphase tilt reflection; i = $^1/_2\{ooe\}$ in-phase tilt reflection; M = $^1/_2\{eeo\}$ with contributions from antiparallel cation displacements; and AO_1 = short-range A-site vacancy order.

Table 2. Summary of Electron Diffraction Results for $Sr_{1-3x/2}La_xTiO_3$ Ceramics Sintered in Air and N_2/5% H_2

composition	$x = 0.30$		$x = 0.50$		$x = 0.63$	
atmosphere	air	N_2/5% H_2	air	N_2/5% H_2	air	N_2/5% H_2
antiphase tilt	√	√	√	√	√	√
in-phase tilt	×	×	√	×	√	√
A-site ordering	short	×	long	short	long	long

formation of V_O in the former. First, V_O disrupts the cogwheel-like correlation of octahedral rotations and decreases the driving force for the onset of octahedral tilt transitions. This effect has been elegantly demonstrated in a range of doped $SrTiO_3$ compositions by Tkach et al. and shown to be a universal principle in all octahedral framework compounds such as tetragonal tungsten bronzes by Zhu et al.[35,36] Second, the formation of V_O will be accompanied by the creation of Ti^{3+}. A distribution of V_O and Ti^{3+} ions throughout the lattice resulting from reduction in N_2/5% H_2 could potentially decrease the total number of A-site vacancies by facilitating direct compensation of La^{3+} through electrons (Ti^{3+}). We note, however, that reduction in N_2/5% H_2 may also decrease the driving force for A-site vacancy order by creating a B- and O-site defect distribution that coexists with the A-site distribution and disrupts the conventional charge- and strain-related driving forces for order. Irvine et al. have reported the precipitation of TiO_2 from A-site-deficient $Sr_{1-3x/2}La_xTiO_{3-\delta}$ porous ceramics on annealing at ~1000 °C under reducing conditions, thus supporting the suggestion of fewer than expected A-site vacancies for samples prepared under reducing conditions.[23,37]

Dark and bright field images obtained under similar conditions to those described in Figure 4 were also obtained for samples that had been sintered in N_2/5% H_2. Antiphase boundaries associated with antiphase rotations of the O octahedra were routinely observed, but strong contrast arising from large ferroelastic twin domains could not be routinely observed, suggesting that, even for $x = 0.63$, samples sintered in N_2/5% H_2 are not strongly distorted away from cubic, consistent with the XRD data shown in Figure 1.

A summary of electron diffraction results on $Sr_{1-3x/2}La_xTiO_3$ ceramics sintered in air and N_2/5% H_2 is shown in Table 2.

3.3. Thermogravimetric Data. The onset temperature of oxygen uptake decreased with increasing La concentration (Figure 9). $x \leq 0.20$ prepared in N_2/5% H_2 were extremely stable in air even at 1000 °C. Therefore, only TGA data for $x = 0.00$ and 0.20 are reported here. $x \leq 0.20$ remained black after analysis, consistent with limited O_2 uptake; however, $x \geq 0.30$ became white (Table 3). After TGA, $x = 0.30$, 0.40, 0.50, and 0.60 all exsolved TiO_2, consistent with Irvine et al., who reported that $Sr_{1-3x/2}La_xTiO_3$ perovskites with A-site vacancies are more inclined to exsolve B-site species.[37] This would imply that at least some La^{3+} has been compensated locally in the perovkskite lattice through the formation of Ti^{3+} and not entirely through the formation of A-site vacancies, consistent with the observation in ED data (Figure 8) that the onset of the appearance of SRO superstructure occurs at higher values of x for samples sintered in N_2/5% H_2 ($x = 0.50$) compared with those in air ($x = 0.30$).

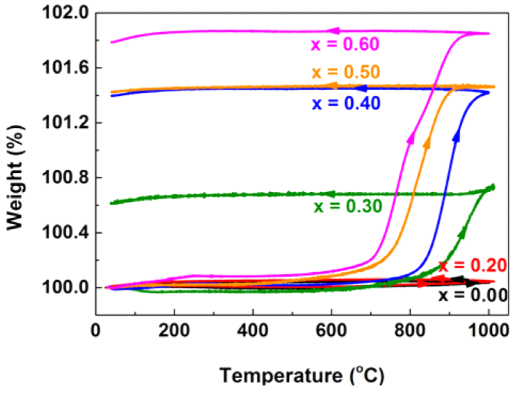

Figure 9. Thermogravimetric analysis showing oxidation in air up to 1000 °C of $Sr_{1-3x/2}La_xTiO_{3-\delta}$ ceramics sintered at 1773 K for 6 h in N_2/5% H_2.

Table 3. Weight Variation, Oxidation Onset Temperature, and Phase Products after TGA of $Sr_{1-3x/2}La_xTiO_{3-\delta}$ Ceramics Sintered at 1773 K for 6 h in N_2/5% H_2

composition	Δwt (%)	oxidation temperature (°C)	products after TGA
$x = 0.30$	0.6	820	TiO_2 + perovskite
$x = 0.40$	1.3	800	TiO_2 + perovskite
$x = 0.50$	1.4	750	TiO_2 + perovskite
$x = 0.60$	1.8	700	TiO_2 + perovskite

3.4. Thermoelectric Data for the N_2/5% H_2-Sintered Samples. S, σ, κ, and ZT for $Sr_{1-3x/2}La_xTiO_{3-\delta}$ ceramics sintered in N_2/5% H_2 at 1773 K for 6 h over a range of different temperature and values of x are shown in Figure 10. Negative S values suggested that all samples are n-type semiconductors. The undoped $SrTiO_3$ sample had very high absolute S; however, it had low σ. $|S|$ became smaller with increasing x (Figure 10a), possibly due to an increase in the carrier concentration (Figure 10b). σ increased at first, reached a maximum, and then decreased with increasing x at $x \leq 0.30$ (Figure 10b). κ decreased with increasing temperature and was ~3 W m^{-1} K^{-1} at 973 K for $x \leq 0.30$ (Figure 10c).

Comparison of ZT at 973 K showed the same trend as σ with temperature and reached a maximum of 0.41 at 973 K for $x = 0.15$ due to its high σ (Figure 10e). For $x \geq 0.40$, S and σ decreased and became too low for thermoelectric applications (Figure 10f,g). A steep decline in σ was observed for $x = 0.40$ and 0.50 (Figure 10g).

The Ti^{3+} content of $x \leq 0.40$ was calculated from an empirical equation for cubic $SrTiO_3$ perovskites as follows

$$a = a_o + 0.063y_{Ti^{3+}}$$

where a and a_0 are the cell parameters for N_2/5% H_2- and air-sintered samples, respectively.[23] As shown in Figure 11, the Ti^{3+} content was found to increase with increasing La concentration up to $x = 0.20$ and then reaches a plateau at $x = 0.30$ and 0.40, whereas σ at 473 K kept rising to $x = 0.175$ and then decreased with increasing La content, suggesting that the σ increase of cubic perovskites with low La content ($x \leq 0.175$) is mainly due to an increase in the carrier concentration.

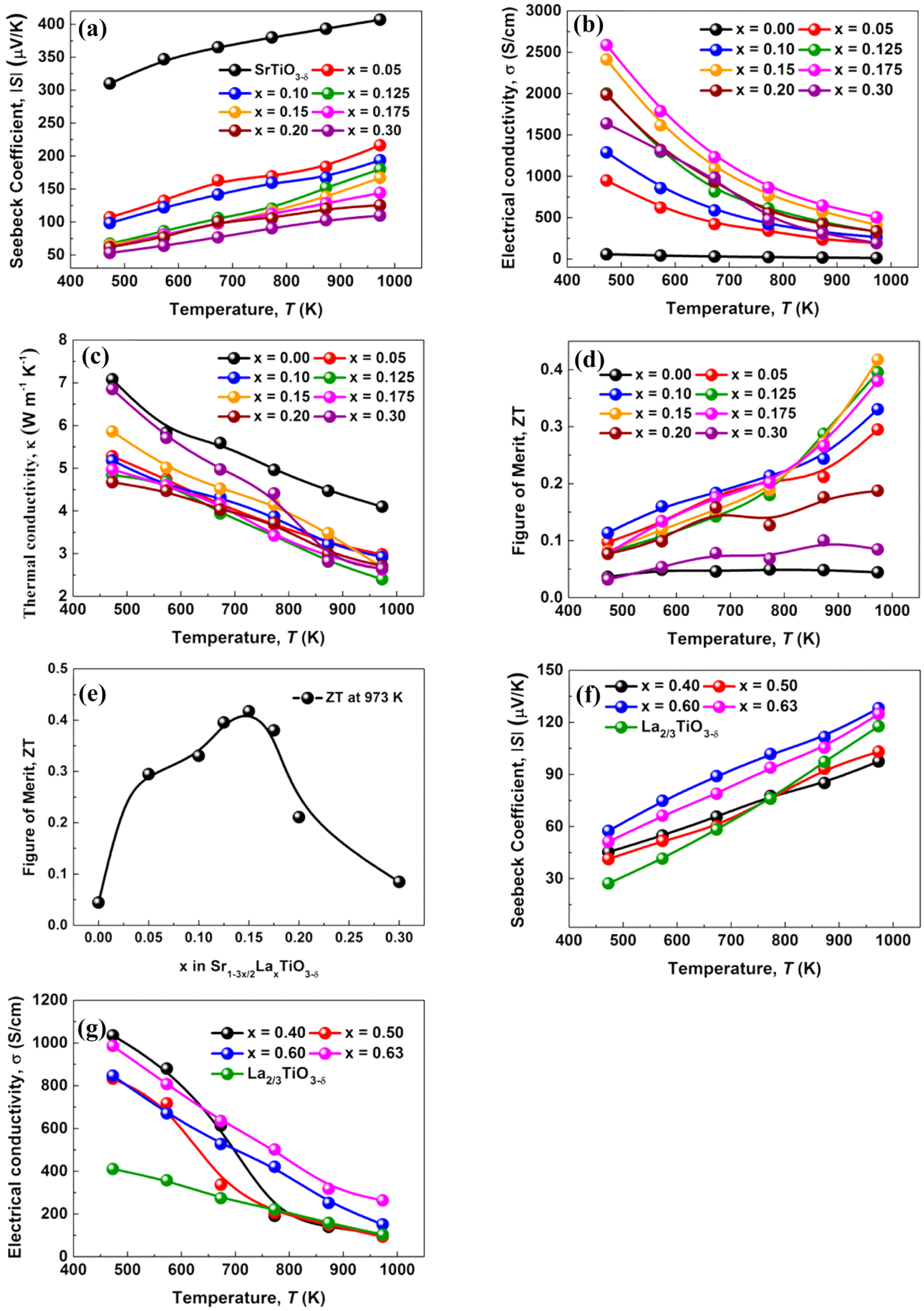

Figure 10. Temperature dependence of (a) |S|, (b) σ, (c) κ, and (d) ZT for $x \leq 0.30$; (e) ZT at 973 K versus x in $Sr_{1-3x/2}La_xTiO_{3-\delta}$ ceramics; (f) |S| and (g) σ for $x \geq 0.40$ ceramics sintered in N_2/5% H_2 at 1773 K for 6 h.

4. DISCUSSION

X-ray diffraction and TEM data revealed a phase transition from a metrically cubic phase to a distorted orthorhombic phase (tilt system $a^-a^-c^+$) at $x = 0.50$ and 0.63 in air- and N_2/5% H_2-sintered samples, respectively. However, ED patterns revealed all samples with $0.10 \leq x < 0.50$ and $0.10 \leq x < 0.63$ in air and N_2/5% H_2, respectively, exhibited reflections consistent with a structure in which the octahedra are rotated in antiphase only, presumably $a^0a^0c^-$ ($I4/mcm$), as proposed by Howard et al.[26] The onset of octahedral tilting has been shown to be sensitive to the concentration of V_O by several authors.[36] V_O disrupt the cogwheel-like correlation of O-octahedral rotations, which results in either a decrease in the onset temperature of the relevant tilt transition or an increase in x before tilting occurs above ambient. The role of A-site vacancies and vacancy

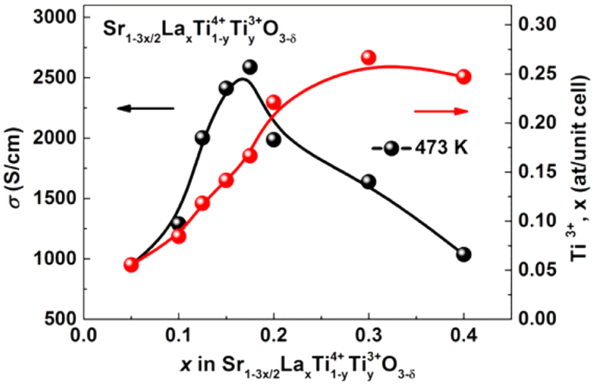

Figure 11. σ versus x at 473 K and Ti^{3+} content versus x in $Sr_{1-3x/2}La_xTiO_{3-\delta}$ ceramics sintered at 1773 K for 6 h in N_2/5% H_2. Ti^{3+} content was calculated from an empirical equation: $a = a_o + 0.063y_{Ti^{3+}}$, where a and a_0 are the cell parameters for N_2/5% H_2- and air-sintered samples, respectively.[23]

order in the onset of structural transitions is less clear. A-site vacancies in the context of tilting may be considered an effective ionic radius that influences the onset of tilting through simple tolerance factor considerations.[38] Ubic et al. have discussed at length the role of A-site vacancies in the onset of structural transitions, and they concluded that the effective ionic radius of the vacancy was similar to the constituent A-site ion and that no significant lowering of tolerance factor was evident and hence there is little effect on the tilt transition temperature.[39]

In addition to the onset of tilting, air-sintered samples revealed a transition from SRO to LRO A-site vacancies as x increased from 0.30 to 0.63, in agreement with work presented by Battle et al.[25] SRO A-site vacancies were evidenced by unique weak diffuse reflections at $^1/_2\{eeo\}$ for samples with x = 0.30. Direct evidence for LRO of A-site vacancies was obtained using atomic resolution HAADF and ABF imaging and inferred through the unusually strong intensities associated with the $^1/_2\{eeo\}$ reflections (in comparison with $^1/_2\{ooe\}$) in ED patterns for samples with $x \geq 0.50$ sintered in air. The $^1/_2\{eeo\}$ reflections are an amalgam of intensity associated with antiparallel cation displacements and A-site vacancy order, whereas discrete $^1/_2\{ooe\}$ reflections arise uniquely from in-phase tilting.

The appearance of A-site vacancy order in samples sintered in N_2/5% H_2 was less clear, with the driving forces for cation/vacancy order (charge and strain) potentially disrupted by additional B- (Ti^{3+}) and O-site (V_O) defects. However, the appearance of TiO_2 and $SrTiO_3$ phases after reoxidation suggests that the concentration of A-site vacancies is lower in samples sintered in N_2/5% H_2 and implies at least some La^{3+} has been incorporated into the lattice through compensation by the formation of Ti^{3+} (electronic compensation). This observation is consistent with the appearance of SRO A-site vacancies for x = 0.50 rather than x = 0.30 for N_2/5% H_2- and air-sintered samples, respectively. To understand this fully, extensive atomistic simulation is required since the experimental data presented strongly suggest that enhancement of thermoelectric properties occurs when all three sites are likely to exhibit charge and strain defects of the type described (A-site and anion vacancies and Ti^{3+} ions).

Optimum thermoelectric properties for $Sr_{1-3x/2}La_xTiO_{3-\delta}$ sintered in N_2/5% H_2 occur for ceramics with $x \approx 0.15$, which represents the best combination of S, σ, and κ. On the basis of an estimated Ti^{3+} content from Figure 11, this corresponds to an approximate composition of $Sr_{0.775}La_{0.15}Ti_{0.86}{}^{4+}Ti_{0.14}{}^{3+}O_{2.93}$. Importantly for applications, compositions with $x \leq 0.20$ are not subject to easy reoxidation, as illustrated by the thermogravimetric data presented in Figure 9, suggesting they are considerably more stable as A-site and oxygen-deficient perovskites and are less prone to exsolving TiO_2 on oxidation compared to that for compositions based on $x > 0.20$.

A combination of a near linear increase in unit cell volume and Ti^{3+} ion content with x for $x \leq 0.20$ (Figures 1c and 11, respectively) indicates the defect chemistry in these compositions is primarily based on the creation of A-site vacancies by La replacing Sr on the A-sites combined with oxygen loss under reducing conditions to create Ti^{3+} ions. The A-site vacancies assist with reducing κ compared to $SrTiO_3$ (Figure 10c), and the Ti^{3+} content is responsible for the strong enhancement of σ, thus resulting in high ZT values of ~0.40 (at 973) for compositions in the range $0.125 \leq x \leq 0.175$. The decrease in unit cell volume (Figure 1c) combined with a leveling off of Ti^{3+} content and a decrease in σ for $x > 0.20$ (Figure 11) are strong indicators of more complex defect chemistry and suggest these perovskites may be kinetically stabilized under the reducing conditions employed to produce the ceramics. The sintering periods were short (ca. 6 h at 1773 K), and there was no evidence of TiO_2 via XRD, ED, or TEM for any of the ceramics sintered under reducing conditions. The rapid oxidation of reduced samples with $x > 0.20$ in air with TiO_2 exsolution below 1000 °C is consistent with the proposal from Irvine et al. that perovskites with significant levels of A-site and O-vacancies are prone to exsolve B-site species and form a perovskite with a composition closer to ABO_3.[37] In the case of the series presented here, reduced ceramics of x = 0.20 have an estimated composition of $Sr_{0.70}La_{0.20}Ti_{0.80}{}^{4+}Ti_{0.20}{}^{3+}O_{2.90}$ and are close to the upper limit of stability toward oxidation in air at 1273 K. Thus, reduced samples with > 10% A-site vacancies and > 3% anion vacancies are thermodynamically unstable in air below 1273 K.

The high degree of reoxidation associated with samples with $x > 0.20$ may relate to the onset of A-site vacancy ordering observed in ED patterns, which, in principle, could create highly favorable diffusion paths for the egress and ingress of oxygen. We note, however, that in N_2/5% H_2-sintered samples there is no significant evidence of SRO for x = 0.30 and superstructure reflections appear only for $x \geq 0.30$. Despite the absence of detectable A-site vacancy superstructure reflections for x = 0.30, it is nonetheless reasonable to consider the increase in concentration of A-site vacancies plays a significant role in reoxidation. According to stoichiometry, reduced x = 0.30 produces 15% A-site vacancies. The development of SRO within the solid solution suggests that, statistically, these vacancies reside on alternate (001) planes, so their effective concentration on the partially vacated planes is > 15%. For $x \geq 0.50$, the concentration of A-site vacancies on the partially vacated (001) planes can exceed 50% for ordered regions. We propose the A-site and anion vacancies create an interconnected 2D array of short circuit diffusion paths through comparatively empty AO_3 perovskite {111} pseudo-close-packed stacking planes, resulting in a rapid increase in the diffusion rate of O. Increasing the La concentration, therefore, increases the number and interconnectivity of these short circuit paths, resulting in rapid reoxidation. In perovskites, grain boundary O diffusion is often considered to dominate over bulk particularly at temperatures significantly lower than that of sintering (e.g., ∼573 K lower), as described extensively for $BaTiO_3$-based positive temperature coefficient thermistors.[40,41] Doubtless, grain boundaries play a role in reoxidation within the present study, but comparison of the thermogravimetric data with grain size does not reveal a systematic trend, and the increase in La concentration (and A-site vacancies) is, therefore, considered to dominate.

At high temperatures, values of thermal conductivity for La-doped composition converge, with only the undoped compositions being significantly higher. There are many factors that influence thermal conductivity, such as point defects, dislocations, and grain boundaries. We note that all of the measured La-doped compositions exhibit octahedral rotations of the O octahedra at room temperature, but it is unclear whether long- or short-range superstructure exists at the temperature at which the thermoelectric properties are optimized. Nonetheless, at 973 K, optimized compositions contain cation and anion vacancies and a distribution of Ti^{3+}/Ti^{4+} that enhance phonon scattering and decrease thermal conductivity.

5. CONCLUSIONS

In conclusion, we report optimized ZT values of 0.41 (at 973 K) for n-type $Sr_{1-3x/2}La_xTiO_{3-\delta}$ ceramics with $0.125 \le x \le 0.175$. This represents the highest reported TE ZT values to date for any perovskite-based $SrTiO_3$ ceramics. This was achieved by careful selection of the starting compositions and close control of the ceramic processing conditions to create defective perovskite lattices containing a combination of A- and O-site vacancies with mixed valent Ti^{3+} and Ti^{4+} on the B-site. Although the optimized materials are highly defective non-stoichiometric perovskites, they are resistant to rapid reoxidation in air up to 1273 K, thus demonstrating their potential for TE applications, e.g., as n-type legs in thermoelectric generators operating at high temperatures. This approach provides a highly promising route to further improve the TE properties of titanate-based perovskites.

■ AUTHOR INFORMATION

Corresponding Author

*E-mail: i.m.reaney@sheffield.ac.uk.

Notes

The authors declare no competing financial interest.

■ ACKNOWLEDGMENTS

We thank the EPSRC for funding EP/L017563/1 and access to the Sorby Centre for Microscopy and Microanalysis to obtain high-resolution images and diffraction data.

■ REFERENCES

(1) Snyder, G. J.; Toberer, E. S. Complex Thermoelectric Materials. *Nat. Mater.* **2008**, *7*, 105−114.

(2) Koumoto, K.; Terasaki, I.; Funahashi, R. Complex Oxide Materials for Potential Thermoelectric Applications. *MRS Bull.* **2006**, *31*, 206−210.

(3) Ohtaki, M. Recent Aspects of Oxide Thermoelectric Materials for Power Generation from Mid-to-high Temperature Heat Source. *J. Ceram. Soc. Jpn.* **2011**, *119*, 770−775.

(4) Ravichandran, J.; Siemons, W.; Oh, D.-W.; Kardel, J. T.; Chari, A.; Heijmerikx, H.; Scullin, M. L.; Majumdar, A.; Ramesh, R.; Cahill, D. G. High-temperature Thermoelectric Response of Double-doped $SrTiO_3$ Epitaxial Films. *Phys. Rev. B: Condens. Matter Mater. Phys.* **2010**, *82*, 165126.

(5) Liu, J.; Wang, C. L.; Su, W. B.; Wang, H. C.; Zheng, P.; Li, J. C.; Zhang, J. L.; Mei, L. M. Enhancement of Thermoelectric Efficiency in Oxygen-deficient $Sr_{1-x}La_xTiO_{3-\delta}$ Ceramics. *Appl. Phys. Lett.* **2009**, *95*, 162110.

(6) Howard, S. A.; Yau, J. K.; Anderson, H. U. Structural Characteristics of $Sr_{1-x}La_xTiO_{3+\delta}$ as A Function of Oxygen Partial Pressure at 1400 °C. *J. Appl. Phys.* **1989**, *65*, 1492−1498.

(7) Muta, H.; Kurosaki, K.; Yamanaka, S. Thermoelectric Properties of Rare Earth Doped $SrTiO_3$. *J. Alloys Compd.* **2003**, *350*, 292−295.

(8) Ohta, S.; Nomura, T.; Ohta, H.; Hirano, M.; Hosono, H.; Koumoto, K. Large Thermoelectric Performance of Heavily Nb-Doped $SrTiO_3$ Epitaxial Film at High Temperature. *Appl. Phys. Lett.* **2005**, *87*, 092108.

(9) Cui, Y.; Salvador, J. R.; Yang, J.; Wang, H.; Amow, G.; Kleinke, H. Thermoelectric Properties of Heavily Doped n-Type $SrTiO_3$ Bulk Materials. *J. Electron. Mater.* **2009**, *38*, 1002−1007.

(10) Kikuchi, A.; Okinaka, N.; Akiyama, T. A Large Thermoelectric Figure of Merit of La-doped $SrTiO_3$ Prepared by Combustion Synthesis with Post-spark Plasma Sintering. *Scr. Mater.* **2010**, *63*, 407−410.

(11) Liu, J.; Wang, C. L.; Su, W. B.; Wang, H. C.; Li, J. C.; Zhang, J. L.; Mei, L. M. Thermoelectric Properties of $Sr_{1-x}Nd_xTiO_3$ Ceramics. *J. Alloys Compd.* **2010**, *492*, L54−L56.

(12) Okinaka, N.; Zhang, L.; Akiyama, T. Thermoelectric Properties of Rare Earth-doped $SrTiO_3$ Using Combination of Combustion Synthesis (CS) and Spark Plasma Sintering (SPS). *ISIJ Int.* **2010**, *50*, 1300−1304.

(13) Shang, P. P.; Zhang, B. P.; Liu, Y.; Li, J. F.; Zhu, H. M. Preparation and Thermoelectric Properties of La-Doped $SrTiO_3$ Ceramics. *J. Electron. Mater.* **2011**, *40*, 926−931.

(14) Wang, N.; Li, H.; Ba, Y.; Wang, Y.; Wan, C.; Fujinami, K.; Koumoto, K. Effects of YSZ Additions on Thermoelectric Properties of Nb-Doped Strontium Titanate. *J. Electron. Mater.* **2010**, *39*, 1777−1781.

(15) Wang, H. C.; Wang, C. L.; Su, W. B.; Liu, J.; Sun, Y.; Peng, H.; Mei, L. M. Doping Effect of La and Dy on the Thermoelectric Properties of $SrTiO_3$. *J. Am. Ceram. Soc.* **2011**, *94*, 838−842.

(16) Popuri, S. R.; Scott, A. J. M.; Downie, R. A.; Hall, M. A.; Suard, E.; Decourt, R.; Pollet, M.; Bos, J.-W. G. Glass-like Thermal Conductivity in $SrTiO_3$ Thermoelectrics Induced by A-site Vacancies. *RSC Adv.* **2014**, *4*, 33720−33723.

(17) Kovalevsky, A. V.; Yaremchenko, A. A.; Populoh, S.; Weidenkaff, A.; Frade, J. R. Effect of A-Site Cation Deficiency on the Thermoelectric Performance of Donor-Substituted Strontium Titanate. *J. Phys. Chem. C* **2014**, *118*, 4596−4606.

(18) Kovalevsky, A. V.; Populoh, S.; Patrício, S. G.; Thiel, P.; Ferro, M. C.; Fagg, D. P.; Frade, J. R.; Weidenkaff, A. Design of $SrTiO_3$-Based Thermoelectrics by Tungsten Substitution. *J. Phys. Chem. C* **2015**, *119*, 4466−4478.

(19) Balachandran, U.; Eror, N. G. Electrical Conductivity in Lanthanum-doped Strontium Titanate. *J. Electrochem. Soc.* **1982**, *129*, 1021−1026.

(20) Odekirk, B.; Balachandran, U.; Eror, N. G.; Blakemore, J. S. Conductivity of Strongly Reduced and Quenched Ceramic La-Doped $SrTiO_3$. *J. Am. Ceram. Soc.* **1983**, *66*, C22−C23.

(21) Flandermeyer, B. F.; Agarwal, A. K.; Anderson, H. U.; Nasrallah, M. M. Oxidation-reduction Behaviour of La-doped $SrTiO_3$. *J. Mater. Sci.* **1984**, *19*, 2593−2598.

(22) Muta, H.; Kurosaki, K.; Yamanaka, S. Thermoelectric Properties of Reduced and La-doped Single-crystalline $SrTiO_3$. *J. Alloys Compd.* **2005**, *392*, 306−309.

(23) Neagu, D.; Irvine, J. T. S. Structure and Properties of $La_{0.4}Sr_{0.4}TiO_3$ Ceramics for Use as Anode Materials in Solid Oxide Fuel Cells. *Chem. Mater.* **2010**, *22*, 5042−5053.

(24) Aljaberi, A. D.; Irvine, J. T. S. Ca-substituted, A-site deficient perovskite $La_{0.2}Sr_{0.7}TiO_3$ as A Potential Anode Material for SOFCs. *J. Mater. Chem. A* **2013**, *1*, 5868−5874.

(25) Battle, P. D.; Bennett, J. E.; Sloan, J.; Tilley, R. J. D.; Vente, J. F. A-Site Cation-Vacancy Ordering in $Sr_{1-3x/2}La_xTiO_3$: A Study by HRTEM. *J. Solid State Chem.* **2000**, *149*, 360−369.

(26) Howard, C. J.; Lumpkin, G. R.; Smith, R. I.; Zhang, Z. Crystal Structures and Phase Transition in the System $SrTiO_3$−$La_{2/3}TiO_3$. *J. Solid State Chem.* **2004**, *177*, 2726−2732.

(27) Akin, I.; Li, M.; Lu, Z. L.; Sinclair, D. C. Oxygen-loss in A-site Deficient $Sr_{0.85}La_{0.10}TiO_3$ Perovskite. *RSC Adv.* **2014**, *4*, 32549−32554.

(28) Savaniu, C.-D.; Irvine, J. T. S. Reduction Studies and Evaluation of Surface Modified A-site Deficient La-doped $SrTiO_3$ as Anode Material for IT-SOFCs. *J. Mater. Chem.* **2009**, *19*, 8119−8128.

(29) Savaniu, C.-D.; Miller, D. N.; Irvine, J. T. S.; Menon, M. Scale Up and Anode Development for La-Doped $SrTiO_3$ Anode-Supported SOFCs. *J. Am. Ceram. Soc.* **2013**, *96*, 1718−1723.

(30) Bérardan, D.; Byl, C.; Dragoe, N. Influence of the Preparation Conditions on the Thermoelectric Properties of Al-Doped ZnO. *J. Am. Ceram. Soc.* **2010**, *93*, 2352−2358.

(31) Byl, C.; Bérardan, D.; Dragoe, N. Experimental Setup for Measurements of Transport Properties at High Temperature and under Controlled Atmosphere. *Meas. Sci. Technol.* **2012**, *23*, 035603.

(32) Shannon, R. D. Revised Effective Ionic Radii and Systematic Studies of Interatomie Distances in Halides and Chaleogenides. *Acta Crystallogr., Sect. A: Cryst. Phys., Diffr., Theor. Gen. Crystallogr.* **1976**, *32*, 751−767.

(33) Woodward, D. I.; Reaney, I. M. Electron Diffraction of Tilted Perovskites. *Acta Crystallogr., Sect. B: Struct. Sci.* **2005**, *61*, 387−399.

(34) Glazer, A. M. The Classification of Tilted Octahedra in Perovskites. *Acta Crystallogr., Sect. B: Struct. Crystallogr. Cryst. Chem.* **1972**, *28*, 3384−3392.

(35) Tkach, A.; Vilarinho, P. M.; Kholkin, A. L. Structure−microstructure−dielectric Tunability Relationship in Mn-doped Strontium Titanate Ceramics. *Acta Mater.* **2005**, *53*, 5061−5069.

(36) Zhu, X.; Fu, M.; Stennett, M. C.; Vilarinho, P. M.; Levin, I.; Randall, C. A.; Gardner, J.; Morrison, F. D.; Reaney, I. M. A Crystal-Chemical Framework for Relaxor versus Normal Ferroelectric Behavior in Tetragonal Tungsten Bronzes. *Chem. Mater.* **2015**, *27*, 3250−3261.

(37) Neagu, D.; Tsekouras, G.; Miller, D. N.; Ménard, H.; Irvine, J. T. S. In Situ Growth of Nanoparticles through Control of Non-stoichiometry. *Nat. Chem.* **2013**, *5*, 916−923.

(38) Reaney, I. M.; Ubic, R. Dielectric and Structural Characteristics of Perovskites and Related Materials as A Function of Tolerance Factor. *Ferroelectrics* **1999**, *228*, 23−38.

(39) Ubic, R.; Subodh, G.; Sebastian, M. T.; Gout, D.; Proffen, T. Structure of Compounds in the $Sr_{1-3x/2}Ce_xTiO_3$ Homologous Series. *Chem. Mater.* **2008**, *20*, 3127−3133.

(40) Nowotny, J.; Rekas, M. Positive Temperature Coefficient of Resistivity for $BaTiO_3$-based Materials. *Ceram. Int.* **1991**, *17*, 227−241.

(41) Brutchey, R. L.; Cheng, G.; Gu, Q.; Morse, D. E. Positive Temperature Coefficient of Resistivity in Donor-Doped $BaTiO_3$ Ceramics Derived from Nanocrystals Synthesized at Low Temperature. *Adv. Mater.* **2008**, *20*, 1029−1033.

DOI: 10.1021/acs.chemmater.5b04616
Chem. Mater. 2016, 28, 925−935